## Journal of Materials Chemistry A



## **PAPER**

View Article Online
View Journal | View Issue



Cite this: J. Mater. Chem. A, 2025, 13, 30467

# Growth of cylindrical micelles and their use to prepare porous materials with tailored dimensions and alignment

Mengxue Zhang, D Xiaomeng Li, D Chuanbing Tang D and Morgan Stefik D\*

Materials with cylindrical pores are optimal for electrochemical devices and filtration due to their straight paths with minimal tortuosity when aligned. Polymer templates have led to many individual cylindrical architectures however the independent tailoring of pore and wall dimensions has remained elusive. Here short cylindrical micelle templates (PEO-b-PS) with glassy cores enabled the fabrication of sample series with constant cylindrical pore diameter ( $\sim$ 63 nm) and tailored wall thickness (TiO $_2$ ,  $\sim$ 45–100 nm). This ShortCyl series (aspect ratio 4.25) had modest alignment that was attributed to the low free-energy cost for misalignment. Though the plasticized micelles (DCM present) were kinetically trapped while quiescent, an agitation based growth process was found to elongate the cylindrical micelles (aspect ratio 15.1) and was consistent with a surface-limited process. After vitrification, a series of LongCyl samples were templated that exhibited enhanced alignment while also enabling independent control of pore and wall dimensions. Geometric models were derived for aligned cylinders (2D PMT model) and non-aligned cylinders (3D PMT model), however orientation order parameters were better able to distinguish the extent of cylinder alignment. These results highlight how innovative micellization and self-assembly methods enable diverse architectures with tailored extent of alignment.

Received 19th May 2025 Accepted 11th August 2025

DOI: 10.1039/d5ta04040j

rsc.li/materials-a

#### Introduction

Porous materials are broadly used for separations,<sup>1-4</sup> energy storage<sup>5-7</sup> and controlled molecule/solvent transport channels,<sup>8-10</sup> all of which are applications requiring transport. The architecture naturally determines the transport time within a phase. Tortuosity quantifies path-inefficiency as the ratio of the length travelled with respect to the linear offset distance; notably, tortuosity has a minimal value of 1.0 for linear transport. From a device perspective, it is ideal to minimize tortuosity by using anisotropic materials with a high-degree of pore alignment along the transport direction where several optoelectronic examples have identified faster and longer-range transport advantages.<sup>6,11</sup> The advantages of low-tortuosity upon transport and overpotentials were covered in detail previously.<sup>5,12,13</sup>

Materials with cylindrical pores have been pursued by multiple avenues. Cylindrical materials have been replicated from natural wood though the feature sizes are constrained by template diversity. Block polymer strategies have been widely examined using self-assembly. For example cylindrical block polymer phases with an etchable block have been used as templates to prepare porous materials. Also block polymer coassembly has led to the direct assembly of functional

Department of Chemistry and Biochemistry, University of South Carolina, Columbia, SC, 29208, USA. E-mail: morgan@stefikgroup.com

materials with cylindrical pores.21-24 The noted block polymer methods were based on equilibration where independent feature size tailoring is limited and challenging, e.g. changing the polymer molecular mass convolves changes to both the pore size and wall thickness simultaneously.25 The alignment of cylindrical phases is also challenging where viscous flow<sup>26</sup> and electric field alignment<sup>16-19</sup> have resulted in aligned materials but require complex processing. Polymer micelle templates have also been used to prepare porous materials, however cylindrical micelles often have narrow windows of stability27 and can transform into different morphologies during evaporative processing. It was suggested that the free-energy of different micelle morphologies are relatively similar which can lead to morphology mixtures and morphology changes during processing.28 For example, both the micelle size and morphology depend on the solvent conditions and can be altered by the presence of material nanoparticles.27,29-37 Core block crystallization has been used to prepare robust cylindrical micelles with poly(ferrocenyldimethylsilane),38-40 poly(lactide),41 poly(caprolactone),42 and oligo(p-phenylenevinylene)43 however these have not been used to template other materials yet. Thus to date, the independent adjustment of the feature sizes (pores and walls) with aligned cylindrical pores has remained elusive.

These limitations of processing, complexity, and tailorability are largely resolved with persistent micelle templates (PMTs). Here persistent micelles are kinetically trapped templates are combined with sol–gel material precursors. These kinetically

entrapped micelles maintain constant aggregation number so that the template/pore size is constant. Thus the variation of the material: template ratio enables independent variation of the wall thickness with 2 Å precision control between samples demonstrated elsewhere. 25,44-46 The PMT method has robust guidelines, a geometric model for spherical templates, 45 and kinetic control *via* two modalities: either a χ*N*-barrier or a glassy core. Despite these capabilities, PMT has so far remained limited to spherical micelles. Here we develop glassy core cylindrical micelles of variable length and examine their use to produce tailored architectures with cylindrical pores. In all cases, these cylindrical PMTs enable the independent tailoring of pore size and wall thickness. Furthermore, the extent of cylinder alignment was found to vary with the micelle length. Towards this end, micelle agitation was identified as a route to enhance cylinder length which was attributed to a surfacelimited process. To the best to our knowledge, this is the first example of self-assembling cylindrical pores from polymer

micelle templates with both independently tailorable wall dimensions and extent of alignment.

## **Experimental section**

#### **Materials**

2-Bromopropionic acid (98%, BeanTown Chemical), 4-(dimethylaminopyridine) (DMAP, 99%, Sigma-Aldrich), anhydrous diethyl ether ( $\geq$ 99%, Sigma-Aldrich), anisole (99%, BeanTown Chemical), chloroform (CHCl<sub>3</sub>, >99%, Sigma-Aldrich), chloroform-D (CDCl<sub>3</sub>, 99.8%, Cambridge Isotope Laboratories Inc.), concentrated hydrochloric acid (HCl, 37% w/w, ACS grade, VWR), methylene chloride (DCM, 99%, Fisher Scientific), N,N,N',N'',N'''-pentamethyldiethylenetriamine (PMDETA, >98%, Acros Organics), poly(ethylene glycol) monomethyl ether with molecular weight of 5000 g mol<sup>-1</sup> (PEO<sub>113</sub>–OH, Sigma) and 35 000 g mol<sup>-1</sup> (PEO<sub>795</sub>–OH, Alfa Aesar), titanium tetraisopropoxide (TTIP, 99% Acros Organics) were used as received.

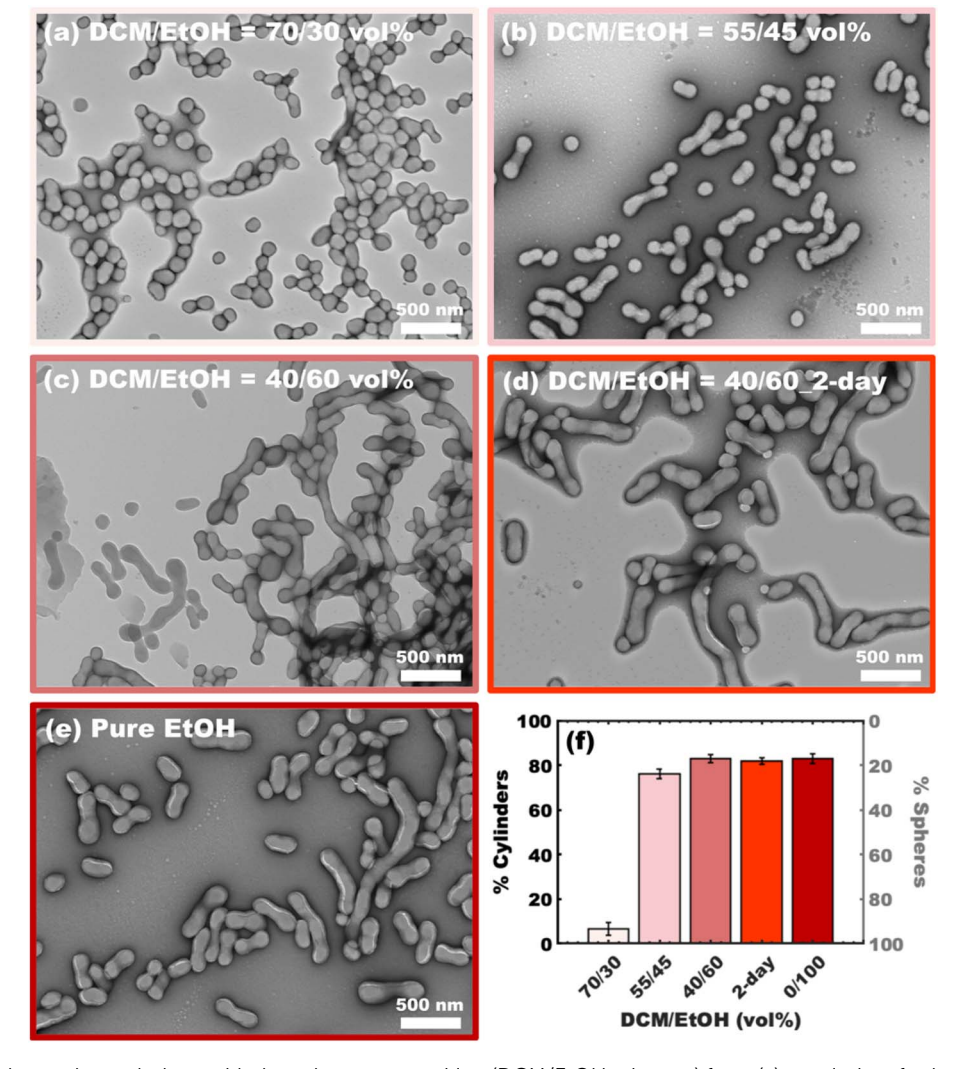


Fig. 1 OS1 micelles changed morphology with the solvent composition (DCM/EtOH mixtures) from (a) a majority of spheres to (b) a majority of short cylinders followed by (c and d) apparent kinetic entrapment prior to (e) vitrification of the PS core in pure EtOH (non-solvent). The (f) number fraction of spheres/cylinders for each condition is shown. Representative TEM images shown using UrAc stain (relative brightness of micelles depends on the local concentration of stain).

Ethanol (EtOH, 200 proof, Deacon Labs) and methanol (MeOH, 99.8%, Fisher Scientific) were dried with 50 wt% molecular sieves (3 Å, 8-12 meshm Acros Organics) prior using. Copper(1) bromide (CuBr(1), 99.99%. Aldrich). didodecyldimethylammonium bromide (DDAB, 98%, Tokyo Chemical Industry) were all stored under argon atmosphere. Uranyl acetate solution (UrAc, 1%, Electron Microscopy Sciences) was stored in the refrigerator. Styrene monomer (99%, Acros Organics) was stored in a refrigerator and passed through aluminum oxide columns prior to use. Carbon-coated 300 mesh copper grids were purchased from Electron Microscopy Sciences for TEM measurements.

#### Poly(ethylene oxide-b-styrene) (OS) synthesis

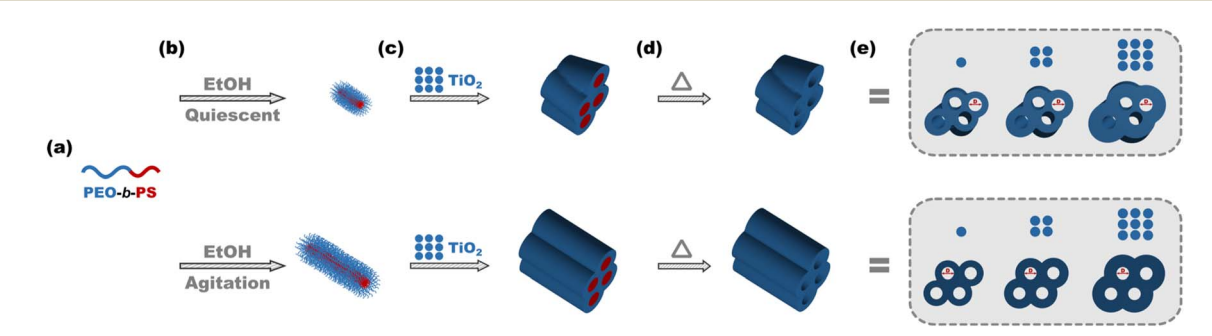
A representative procedure of the diblock copolymer OS1 synthesis is described as follows. The PEO<sub>795</sub>-Br macro-initiator was synthesized via the steglich esterification. PEO<sub>795</sub>-OH (10 g, 1 eq.) was dissolved in 46.5 mL anhydrous MeOH-free chloroform and sparged with N<sub>2</sub> for 10 min, followed by the dropwise addition of 2-bromopropionic acid (87.4 mg, 2 eq.). The reaction solution was then set in the ice bath. Next, DMAP (28 mg, 0.8 eq.) and DCC (118 mg, 2 eq.) were dissolved in 1 mL and 2.5 mL anhydrous chloroform separately, dropwise added into PEO<sub>795</sub>-OH reaction solution in sequence. The suspension was allowed to stir overnight before purification. The crude product was

collected via gravity filtration to remove the urea by-product. The filtrate was precipitated in cold diethyl ether twice to remove un-reacted PEO<sub>795</sub>-OH. The macro-initiator was then obtained by vacuum filtration and completely dried in a vacuum chamber overnight.

Next the PEO<sub>795</sub>-Br macro-initiator (3 g, 1 eq.), inhibitor free styrene (8.28 g, 928 eq.) and anisole (32 mL) were mixed in a Schlenk flask. After 3 cycles of freeze-pump-thaw to remove oxygen, the solution was brought into the glovebox. A copper stock solution was prepared in the glovebox by dispersing CuBr(1) (0.0645 g, 0.45 mmol) and PMDETA (0.0949 mL, 0.45 mmol) with 0.9 mL anisole in a 1-dram vial. After adding 0.190 mL of the copper stock solution to the polymerization vessel, the Schlenk flask was immersed in a preheated oil bath at 110 °C. After 6 h, the polymerization was stopped by cooling the flask to room temperature and exposing its contents to air. The OS1 was purified by passing it through an aluminum oxide column followed by precipitation in cold methanol three times, filtration and vacuum drying overnight. These conditions resulted in 90% monomer conversion.

#### Polymer characterization

Proton nuclear magnetic resonance (<sup>1</sup>H-NMR) spectroscopy was used to determine the molecular weight fractions of diblock copolymers (Bruker Avance III HD 400 MHz). Chemical shifts



Scheme 1 (a) PEO-b-PS was used to prepare (b) persistent cylindrical micelles (glassy core) with varied cylinder length by altering the agitation time. These cylinders were used as (c) templates for TiO<sub>2</sub> nanoparticles in the preparation of (d) mesoporous materials with cylindrical pores. The (e) variation of the TiO<sub>2</sub>: micelle fractions ("material: template ratio") tailored the wall-thickness alone while preserving constant micelles size and shape.

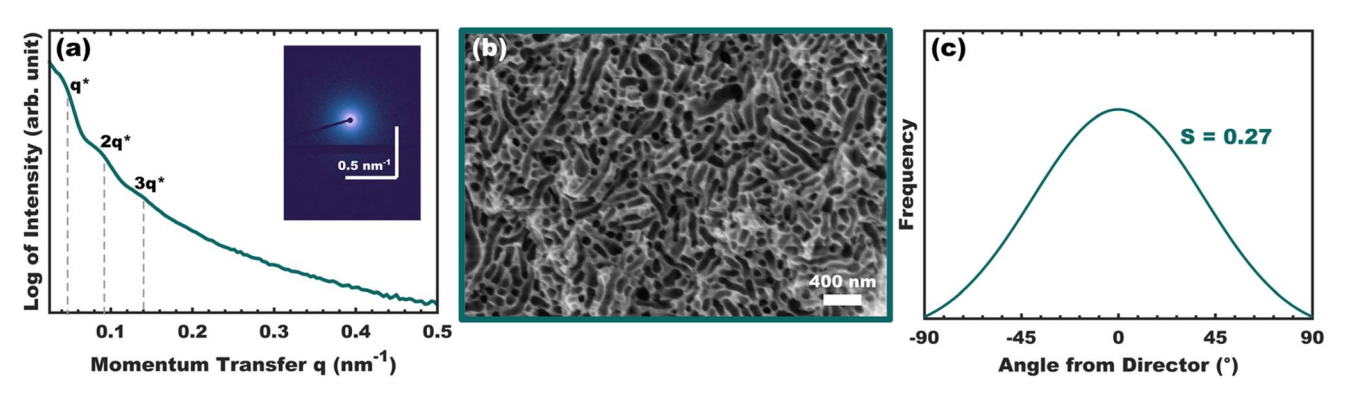


Fig. 2 Representative sample ShortCyl-2.2 made using OS1 polymer showing (a) integrated SAXS pattern with inset 2D pattern and (b) SEM image after calcination where light-regions are TiO<sub>2</sub> and dark regions are pores (prior position of micelle templates). (c) The cylinder orientation distribution was measured using SEM and the histogram best-fit is presented with the corresponding orientation order parameter.

were reported in ppm with TMS as an internal standard (TMS 0.00 ppm for <sup>1</sup>H).

Gel permeation chromatography (GPC) was employed to identify the molar mass dispersity (D) of diblock copolymers using a Varian 390-LC system. A refractive index detector and three PLgel 10  $\mu$ m mixed-BLS columns (300  $\times$  7.5 mm) were used with THF eluent at 30 °C with 1.0 mL min<sup>-1</sup> of flow rate. The GPC system was calibrated with polystyrene (PS) standards provided by PSS Laboratories. The D analysis was calculated using PSS WinGPC UniChrom software V 8.33, Build 9050.

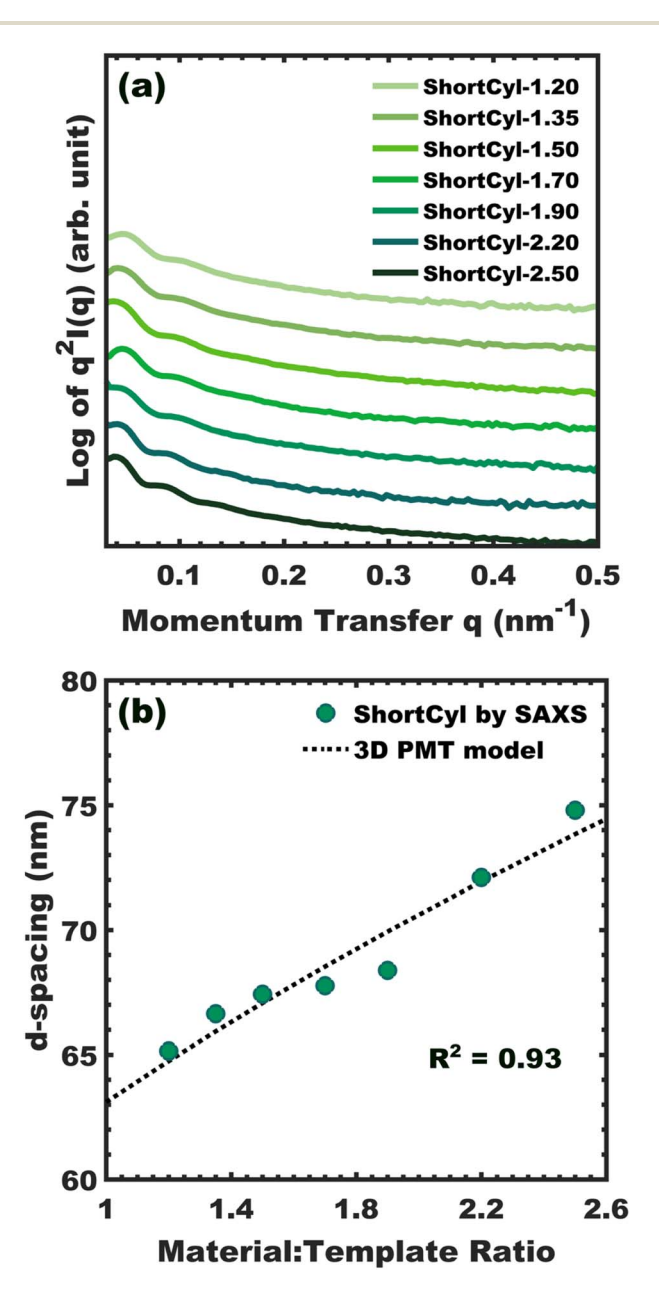


Fig. 3 (a) SAXS data from the ShortCyl series where increasing the material: template ratio shifted all peaks to lower-q. The (b) *d*-spacing of the second SAXS peak had minimal overlap with the beam stop and was used to track lattice expansion quantitatively. Similar quality fits were feasible with both the 2D and 3D PMT model where the 3D model is presented to match the modest extent of cylinder alignment (Fig. 2). The micelles were made using OS1 polymer.

#### Thermal property characterization

Differential scanning calorimeter (DSC, Hitachi 7020) was used to analyze the glass transition temperature ( $T_{\rm g}$ ) of OS polymers. Thermogravimetric analysis system (TGA, Hitachi 7200) was used to analyze the decomposition temperature ( $T_{\rm d}$ ) of OS polymers.

#### Short cylindrical micelle (ShortCyl) preparation

5 mg of OS1 was dissolved in 1 mL DCM followed by 2.5 h of shaking (agitation) at 250 rpm. EtOH was then added dropwise with 10 vol% increments with 2.5 h of quiescent sitting between additions until reaching 60 vol% of EtOH. Next, the ShortCyl solution was quenched with a 20:1 excess of EtOH with the intention of vitrifying the micelles. Rotary evaporation was used to remove non-selective solvent (DCM) until reaching a concentration of 5 mg mL $^{-1}$ .

#### Long cylindrical micelle (LongCyl) preparation

5 mg of OS1 was dissolved in 1 mL DCM followed by shaking (agitation) at 250 rpm for 2.5 h. EtOH was then added gradually with 10 vol% increments. Fig. 6 shows the effect of agitation time (0, 1, 2.5 h) between each EtOH addition, up to 60 vol%. The micelles for the LongCyl series (Fig. 7) were prepared using 2.5 h of agitation between each EtOH addition, up to 60 vol%. Next, these micelle solutions were quenched with a  $20\times$  excess of EtOH and rotary evaporated to a final concentration of 5 mg mL<sup>-1</sup>, naturally removing DCM during this process.

#### TiO<sub>2</sub> sol-gel synthesis

A  ${
m TiO_2}$  nanoparticle stock solution was prepared using *ex situ* TTIP hydrolysis. The detailed synthesis is described elsewhere. <sup>44</sup> In brief, 1 mL of TTIP was mixed with 0.25 mL of HCl (aq), followed by stirring at 800 rpm for 3 min. Next, 0.4 mL of MeOH was added to dilute the sol solution and stirred for additional 20 min before use.

#### Use of micelle templates to prepare porous materials

The  ${\rm TiO_2}$  nanoparticle stock solution was combined with 0.5 mL of cylinder micelle stock solution with predetermined material: template ratios. These mass ratios were calculated assuming full conversion of TTIP to  ${\rm TiO_2}$ . Next the combined micellenanoparticle solution was gently mixed and cast into a covered 4 cm diameter Teflon dish. After drying, the resulting sample was aged at 150 °C to promote nanoparticle crosslinking. The samples were next heated to 450 °C and held for 2 h to oxidatively remove the polymer templates.

#### Small-angle X-ray scattering (SAXS) measurements

Samples were analyzed at multiple facilities. SAXS at the University of Tennessee Polymer Characterization Laboratory used a Xenocs Xeuss 3.0 instrument with a HFVL microfocus X-ray source (Xenocs GeniX3D) with a copper target to generate a 0.154 nm wavelength monochromatic beam. 2D scattering patterns was collected with a Pilatus3 R 300 K hybrid detector

(Dectris) with  $172 \times 172 \ \mu\text{m}^2$  nominal pixel dimensions. The SAXS data for the bulk film was acquired with a sample-todetector distance at 1750 mm. Data were radially integrated using Xenocs XSACT software with background subtraction of the Kapton substrates. SAXS at the South Carolina SAXS Collaborative used a SAXSLab Ganesha and a microfocus X-ray source (Xenocs GeniX3D) with a copper target used to generate a 0.154 nm wavelength monochromatic beam. A Pilatus 300 K detector (Dectris) was employed to collect 2D scattering patterns with  $172 \times 172 \,\mu\text{m}^2$  nominal pixel dimensions. To calibrate the scattering vector (q), a National Institute of Standards and Technology (NIST) reference 640c silicon powder was used (2 $\Theta$ = 28.44° where  $2\Theta$  is the total scattering angle). This scattering data was processed to 1D curves using SAXSGUI V2.23.23. The sample degree of orientation was analyzed by aligning the director with the detector plane (maximum anisotropy). The orientation order parameter (S) was calculated as the second Legendre polynomial using SAXS data as shown previously. 47 In brief, the azimuthal intensity distribution (0.104 < q < 0.224nm<sup>-1</sup>) was fitted with a gaussian curve to derive the azimuthal spread as the resulting standard deviation ( $\sigma$ ). This standard deviation was then used to calculate S with eqn (1).

#### Transmission electron microscopy (TEM) measurements

A JEOL 1400 Plus Transmission election microscopy (TEM) was used to image micelles in bright field mode with an accelerating voltage of 120 keV. Samples were prepared with a drop of cylindrical micelle stock place on a carbon-coated TEM grid with drying via rapid air flow. Dried samples were next stained using 1 wt% uranyl acetate (UrAc) solution in contact with the grid for 2 min. A minimum 100 measurements were taken for each sample condition to yield statistically significant metrics. Cylinder aspect ratios were reported with respect to the nominal overall cylinder diameter of 100 nm.

#### Scanning electron microscopy (SEM) measurements

Top-view images of calcined bulk films were captured with a Zeiss Ultraplus thermal field emission scanning electron microscopy (SEM). The images were taken with an accelerating voltage of 5 keV using an in-lens secondary electron detector.

The working distance was consistently maintained at 4 mm with constant magnification used for sample measurements to preserve minimize systematic error. A minimum of 100 measurements of pore diameter and wall thickness were taken for each sample. The wall thicknesses were measured as the diameter of inscribed circles as previously described. 44 Data are presented as average values with the standard error-of-themean. The orientational order parameter S was calculated from SEM data using ImageJ to determine the orientation of numerous cylinders and then fitting the resulting orientation distribution with a gaussian curve. Again, S was calculated using the resulting standard deviation with eqn (1).

## Results and discussions

Polymer structure directing agents (SDAs) have been broadly used to develop porous nanoscale materials. One advantage of this route is that systematic synthetic methods enabled the study of and improvement of functional devices by establishing relationships of the nanostructure to the resulting properties and performance. 25,48 The minimal tortuosity of aligned cylindrical phases makes them particularly advantageous for applications requiring transport.5 However, SDA demonstrations of cylindrical phases to date have not shown the independent tailoring of individual architectural parameters one-at-a-time. Bulk polymer phases are not suitable towards this end due to the "tyranny of the equilibrium"49 where free-energy minimization induces changes to multiple architectural parameters (pore diameter, wall thickness, and morphology) when material precursors are added<sup>50</sup> or the processing conditions change.<sup>22</sup> The PMT approach enables the independent adjustment of pore and wall dimensions by utilizing kinetically entrapped micelles which also maintain constant morphology and size when used as templates.51 Here the kinetic entrapment refers to the constant aggregation number (average number of chains within each micelle). With well-defined pore/template geometry, the material wall thickness can be precisely controlled by changing the fraction of material precursors. Kinetic micelle entrapment is feasible with low  $T_g$  polymers when using a high thermodynamic barrier  $(\chi N)$  to chain exchange. Here  $\chi$  is the effective

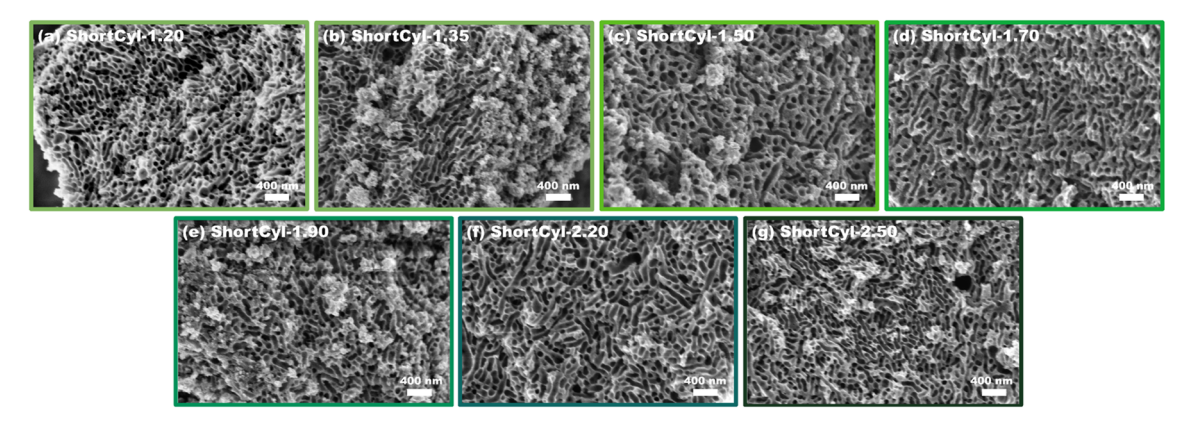


Fig. 4 SEM images ShortCyl series with material: template ratios of (a) 1.20, (b) 1.35, (c) 1.50, (d) 1.70, (e) 1.90, (f) 2.20 and (g) 2.50. The micelles were made using OS1 polymer.

interaction parameter and N scales with the chain length.  $^{44,45,51-53}$  This  $\chi N$  approach to kinetic entrapment however does not appear ideal to preserve non-spherical morphologies since low  $T_{\rm g}$  blocks could reorganize into different micelle shapes regardless of constant aggregation number. Kinetic entrapment of micelle templates is also possible using vitrification which was recently demonstrated with glassy core PMTs.  $^{46,54}$  To date, all PMT demonstrations have been limited to spherical micelles. Here we propose a new strategy using PEO-b-PS (OS) to form cylindrical micelles where the glassy PS core enables both constant micelle diameter and constant micelle shape when used as a template.

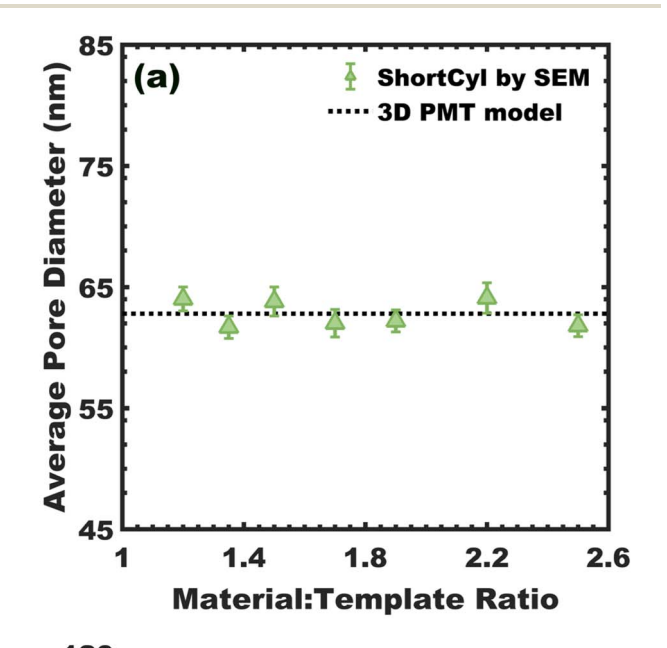
Cylindrical micelles are known to have a narrow processing window in terms of concentration, block fractions, and solvent compositions, in part due to the large differences in polymerselectivity solvent interaction parameters. 27,55,56 Towards this end, a library of 7 different PEO-b-PS polymers were prepared using atomic transfer radical polymerization (ATRP, Fig. S1, S2 and Table S1). Our prior works with PEO-b-PS used EtOH to vitrify micelles from EtOH/DCM mixtures.46,54 Here DCM is a plasticizing and relatively non-selective solvent for PEO-b-PS whereas EtOH induces micellization by increasing  $\gamma$  and eventually leads to kinetic entrapment of chain exchange. Thus the polymer library was screened using such solvent mixtures. The resulting morphologies were checked by TEM where spheres (OS3-7), cylinders (OS1) and precipitation (OS2) were found (Fig. S3). Whereas OS4 yielded spheres, OS1 with similar volume fractions but higher N uniquely led to cylinders. OS1 processing with DCM/MeOH was also briefly investigated where only spheres were found (Fig. S5). The subsequent sections utilize OS1 exclusively to describe (1) the use of short cylindrical micelle templates with glassy cores to produce porous materials with modest alignment and independent tailoring of the wall thickness; (2) a novel agitation-based cylinder-fusion method to produce elongated cylindrical micelles; and (3) the use of these longer cylindrical micelle templates to produce aligned pores.

#### Short cylindrical micelle templates (ShortCyl series)

The formation of OS1 cylindrical micelles was examined as a function of progressive DCM/EtOH mixtures. Aliquots were collected and stained for TEM imaging at each composition. Spherical micelles formed with low EtOH content (30 vol%) whereas a mixture of spheres and cylinders was apparent at 45 vol% EtOH (Fig. 1a and b). Further increasing the EtOH content to 60 vol% increased the cylinder fraction to 83% with some additional elongation apparent with the aspect ratio changing from 3.60 to 4.31 (Fig. 1c). Maintaining this composition quiescently for multiple days led to the same outcome in terms of cylinder fraction, diameter, and aspect ratio of 4.25, suggesting kinetic entrapment (Fig. 1d and S4). The cylindrical micelles were vitrified by quenching the solution to 95 vol% EtOH followed by rotary evaporation of DCM. The micelles were transferred to pure EtOH (vitrified) to preserve both the average core diameter (84.9  $\pm$  3.0 nm error-of-the-mean) and the cylindrical shape (Fig. 1e). Our prior study of PEO-b-PS micelles demonstrated long term 6 month stability at room temperature,

owing to the glassy core.<sup>54</sup> Thus glassy, short cylindrical micelles were prepared for investigation as templates for functional materials.

A series of samples were prepared with different fractions of material precursors around the micelle templates (Scheme 1, top). A single sample is first described in detail before comparing trends within this ShortCyl series. SAXS and SEM data for sample ShortCyl-2.2 (material-to-template ratio of 2.20) are shown in Fig. 2. The SAXS data were isotropic with approximate peak ratios of  $q/q^* \sim 1$ , 2, 3 suggestive of shortrange ordering that was reminiscent of randomly packed structures (Fig. 2a). The corresponding SEM images after



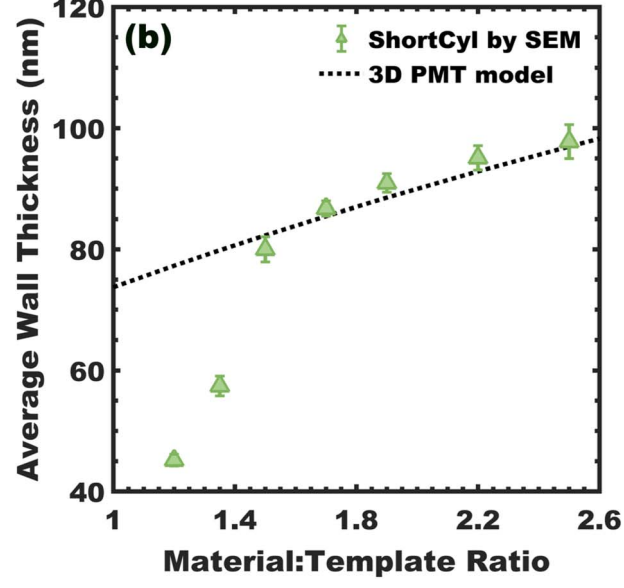


Fig. 5 Analysis of the ShortCyl series where the (a) average pore diameter and (b) average wall thickness were directly measured by SEM and yielded measurements that were consistent with the 3D PMT model best-fit, except for the wall-thickness with M: T=1.20 and 1.35 as noted in the manuscript. The micelles were made using OS1 polymer.

calcination had light regions corresponding to TiO2 and dark regions corresponding to pores where micelle cores were previously located (Fig. 2b). The calcination to 450 °C fully removes the micelle template as validated with TGA measurements (Fig. S4b). Hundreds of locations were measured in the SEM images to derive an average pore diameter 64.1  $\pm$  1.2 nm and an average wall thickness 95.1  $\pm$  2.0 nm. The first SAXS peak corresponded to a  $d_{\text{spacing}}(2\pi/q)$  of 146 nm, approximately matching the sum of core diameter and wall thickness measured by SEM. As expected for a bulk sample, the SEM pore diameter after calcination was ~25% contracted relative to the initial micelle core diameter seen in TEM (Fig. 1e). The extent of cylinder alignment was also determined from SEM images by measuring the orientation distribution of numerous cylinders. The resulting orientation histogram was fitted with a gaussian curve with respect to the dominant direction ("director"). The orientation order parameter S (second order Legendre polynomial) was calculated using:

$$S = \frac{3}{2} \frac{\int_0^{\pi} \exp\left\{\frac{-\Phi^2}{2\sigma^2}\right\} \sin(\Phi)\cos^2(\Phi)d\Phi}{\int_0^{\pi} \exp\left\{\frac{-\Phi^2}{2\sigma^2}\right\} \sin(\Phi)d\Phi} - \frac{1}{2}$$
 (1)

where  $\Phi$  is the integration coordinate with respect to the director ( $\Phi \equiv 0$ ) and  $\sigma$  is the standard deviation (peak width in radians). Here S ranges from 1.0 for perfect alignment to 0 for random, isotropic orientation distributions. Sample ShortCyl-2.2 had S = 0.27 (Fig. 2c), consistent with the broad distribution and limited alignment (full-width-half-max values of  $\sim$ 40°). In summary, these data demonstrate the preservation of the cylindrical micelle shape in the resulting porosity with low extent of alignment.

The complete ShortCyl series was characterized similarly with material-to-template ratios ranging from 1.20 to 2.50 to examine the structural trends. The ShortCyl series SAXS data exhibited a monotonic leftward shift apparent in the corresponding Kratky plot with increasing material:template ratio (Fig. 3a). This increasing  $d_{\rm spacing}$  is consistent with the lattice expansion expected when increasing the material volume in between micelles of constant diameter (Fig. 3b). SEM images from this series all exhibited limited cylinder alignment with constant pore size and increasing wall thickness (Fig. 4). Please note that SEM samples were prepared by pressing powders into carbon tape, thus some fracturing and loose particles are anticipated. Statistical descriptors were calculated from numerous images to identify the relatively constant average pore diameter of  $\sim$ 62.8 nm (Fig. 5a and b). The average wall thickness across the ShortCyl series increased from 45.2  $\pm$ 1.0 nm to 97.8  $\pm$  2.8 nm with increasing material: template ratio (Fig. 5b). Such quantitative trends have been well described by prior PMT models based on sphere packing. However, the packing of cylinders depends on the extent of alignment which results in different scaling laws (see SI 2D/3D PMT models). Both of these new PMT models were able to fit the data well, each having multiple sets of equivocal fit terms that result in similar fit quality. Thus the 3D model was presented for the  $d_{\text{spacing}}$  trend based on the low extent of alignment seen by SEM (Fig. 3b and Table S2). The trend in wall thickness was well fitted for material: template ratios >1.5 with poor fits for ShortCyl-1.2 and ShortCyl-1.35 that were attributed to cylinder jamming with low material loadings (Fig. 5). Thus a set of tailored nanomaterials were prepared with short cylindrical micelle templates with independent adjustment of the wall thickness.

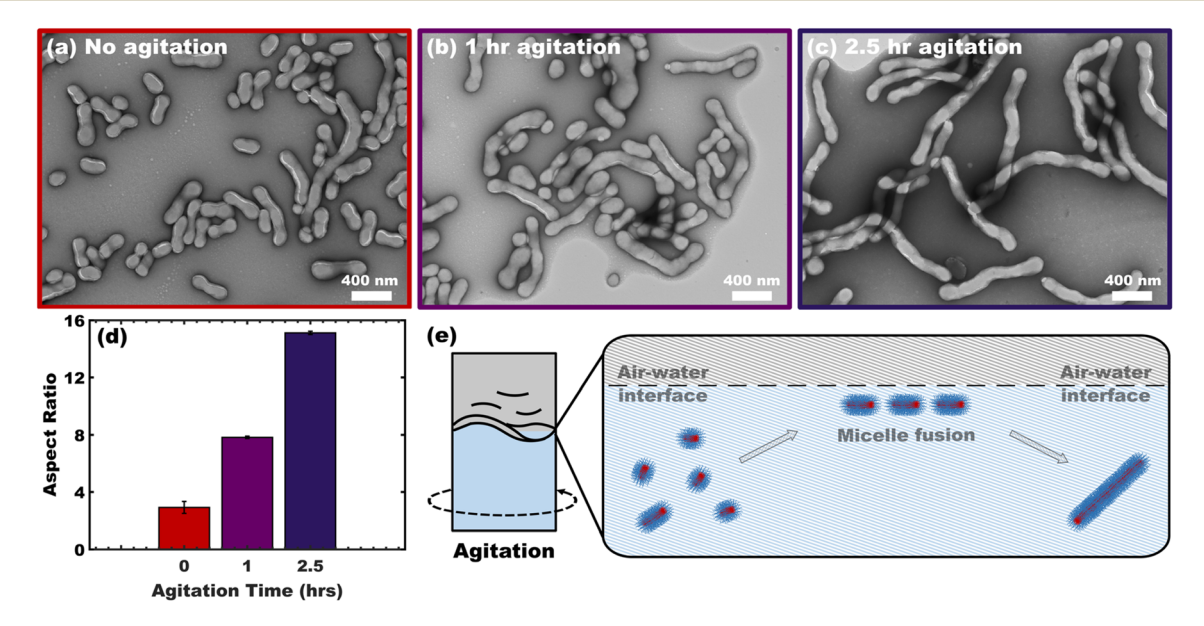


Fig. 6 The cylinder length was constant when (a) quiescent and increased with (b and c) agitation time (shaking) as measured by TEM with UrAc stain. The increasing (d) cylinder aspect ratios quantifies the corresponding cylinder growth. These observations suggest that (e) cylinder growth is associated with turnover of the air-solvent interface during agitation which could drive e.g. micelle fusion. The micelles were made using OS1 polymer with agitation.

#### Agitation-induced cylindrical micelle elongation

A pronounced effect of agitation upon cylindrical micelle formation was noted during this study. The short cylinders

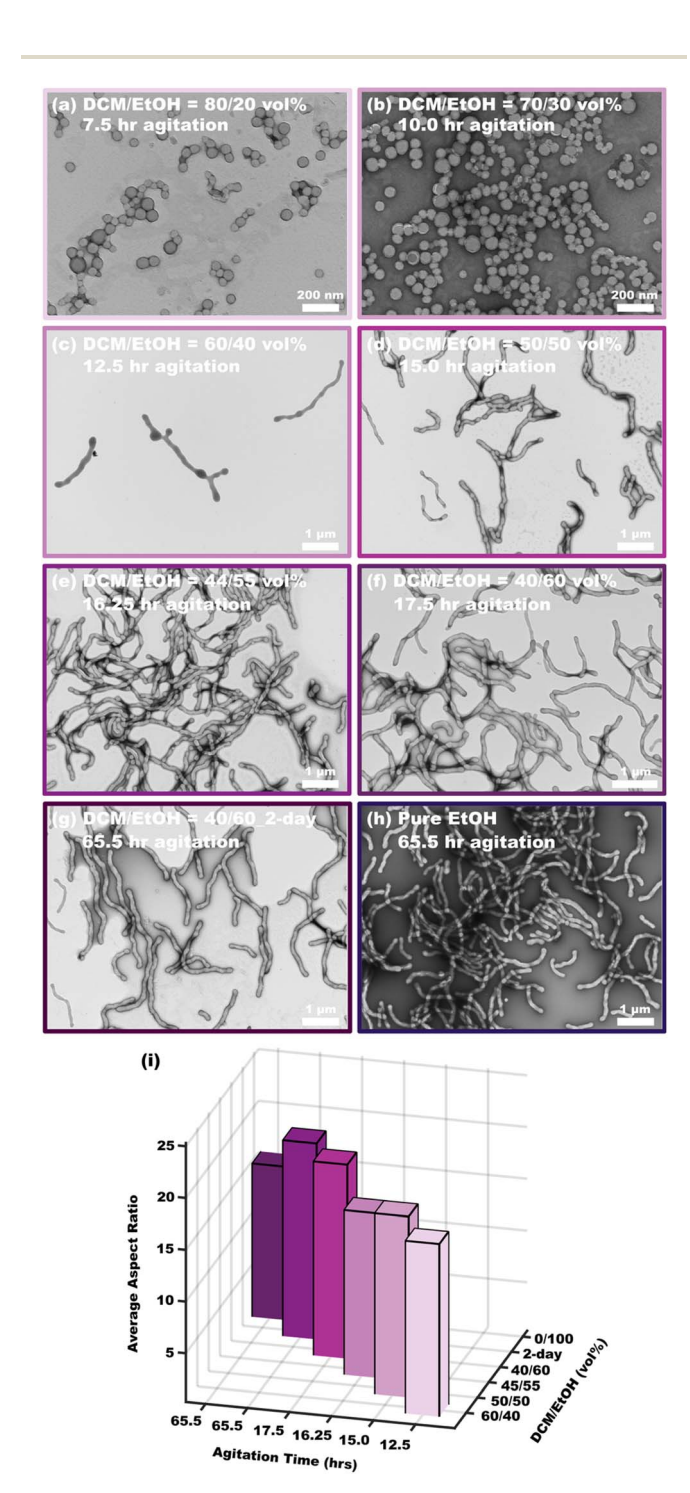


Fig. 7 Shaking and solvent composition changes were used to grow longer cylinders using OS1 polymer. TEM images show the morphology evolution during solvent additions with shaking where (a and b) spheres transition to (c-h) cylinders of increasing length. Cylinder growth is presented as the (i) aspect ratio over time. The micelle length contracts somewhat upon transfer to pure EtOH due to loss of DCM swelling. TEM samples were stained with UrAc where the relative brightness of micelles depends on the local concentrations.

described above were prepared quiescently and resulted in an aspect ratio of 4.25. In contrast, micelles prepared with iterative agitation steps (shaking) led to progressive cylinder growth as apparent in the corresponding TEM images (Fig. 6a-c). Here the aspect ratio increased to 15.1 when 2.5 h of shaking was used between each EtOH addition (Fig. 6d). The TEM images of the resulting micelles included aggregated spheres, early-stage fused micelles that resulted in lumpy cylinders, as well as more homogeneous cylinders (Fig. S6). This sequence of stages is direct evidence consistent with each stage of the proposed mechanism with slow reorganization kinetics. Though time was varied here with constant agitation rate, it is reasonable to expect more rapid agitation would accelerate this process. Indeed, several prior studies identified enhanced micelle exchange mechanisms with agitation<sup>57,58</sup> or cavitation.<sup>59-61</sup> Those prior studies identified the turn-over rate of solution-gas interface as enabling novel exchange processes, possibly via individual chains or possibly via whole micelles adsorbing to the fresh surfaces. Subsequent surface collapse was suggested to either release free chains into the solution or promote collisions for micelle fusion/fission. In this case the TEM data are most consistent with a micelle fusion process (Fig. 6). Micelle fusion is rarely directly observed experimentally, in part attributed to the high activation energy.62 From this perspective, the agitation process used here is uniquely enabling for cylinder growth via fusion.

Agitation induced cylinder growth was utilized further. A 2.5 h agitation step was implemented in between each EtOH addition to enhance cylinder elongation. TEM images were acquired across each of these steps and are shown progressively in Fig. 7. From TEM data, the cylinder length decreased somewhat upon quenching to EtOH, presumably due to the removal of DCM plasticizer which also acts as a swelling agent for the micelle cores. Thus, a novel agitation induced cylinder growth mechanism was identified and used to produce high-aspect ratio cylindrical micelles.

#### Longer cylindrical micelle templates (LongCyl series)

A series of samples were prepared using the long cylindrical micelle templates with different fractions of material precursors (Scheme 1, bottom). A single sample, LongCyl-2.1, is first described in detail before comparing trends. The SAXS pattern of LongCyl-2.1 was again consistent with limited long-range ordering, having broad peaks with approximate q-ratios of  $q/q^* \sim 1$ , 2, 3, consistent with random packing (Fig. 8a). The d-spacing based on the first peak was somewhat larger at  $\sim 132$  nm. The corresponding SEM data revealed a greater extent of cylinder alignment with  $60.2 \pm 1.1$  nm average pore diameters and  $102.1 \pm 3.1$  nm average wall thickness (Fig. 8b). Again, the pore diameter was similarly contracted after calcination as compared to the starting cylinder core size observed in TEM (Fig. 7h). Also the d-spacing was similar to the sum of the pore diameter and the wall thickness.

An earlier hypothesis was that the limited alignment of the short cylinders was due to a minor free-energy cost for nonalignment. In contrast, long cylindrical micelles should have

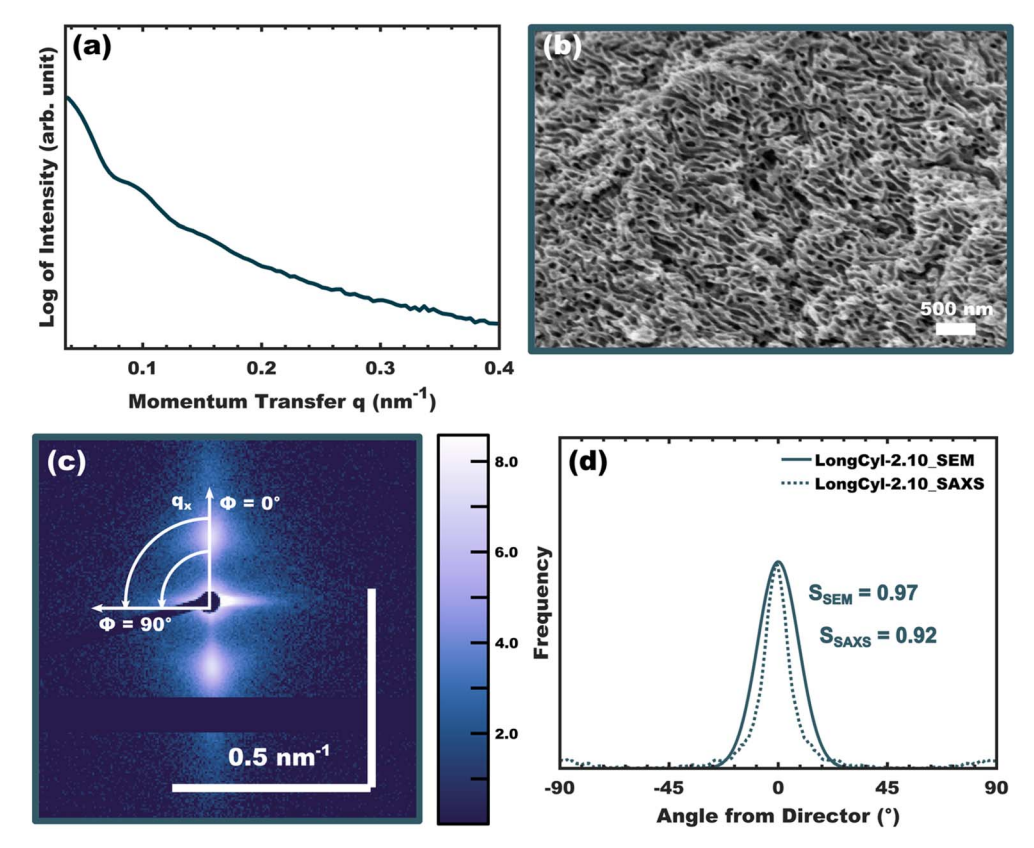


Fig. 8 Representative sample LongCyl-2.1 showing (a) integrated SAXS pattern and (b) SEM image after calcination. 2D SAXS data (c) were measured with the director coplanar with the detector and the (d) cylinder orientation distribution was determined from the azimuthal intensity profile (0.104 < q < 0.224, white arrows) as well as from SEM image analysis. The corresponding orientation order parameters S are indicated. The micelles were made using OS1 polymer with agitation.

a higher free-energy cost for non-alignment which would favor improved alignment to minimize packing disruptions. To examine this hypothesis, the orientation order parameter S was calculated using both SAXS and SEM data. The distribution of azimuthal intensity in 2D SAXS corresponds to the extent of preferred cylinder alignment (Fig. 8c). In brief, the sample was rotated during SAXS until the director laid within the detector plane (maximum anisotropy). Given the proximity of the first peak to the beam stop, the anisotropy was most apparent in the convolution of the second/third peak. The resulting azimuthal intensity profile was fitted with a gaussian curve where eqn (1) was used to calculate the orientation order parameter of S =0.92 (Fig. 8d). A similar value was determined by analysis of the orientation distribution within SEM data which indicated  $\sim 8.5^{\circ}$ full-width half-max relative to the director that corresponded similarly to S = 0.97 (Fig. 8d). This high degree of alignment for long cylinders is perhaps surprising considering that bulk polymer cylindrical phases do not align similarly unless external fields bias the self-assembly. This is in part attributable to the cylinder flexibility when using low  $T_g$  blocks which adapt to unit cell alignment changes with minor free-energy cost. In contrast, the glassy-core cylindrical micelles used here are rigid where cylinder misalignment leads to impingement upon neighboring micelles. This is in contrast to simulations of rigid cylinder packing that have suggested random placement and random orientation as the typical outcome. 63,64 The difference

here may be due to the spacing imposed by corona block interactions as combined with the mobile volume occupied by the material precursors.

The LongCyl series was prepared with material-to-template ratios spanning from 1.00 to 2.10 and were characterized with SAXS and SEM (Fig. 9 and 10). The SEM images revealed relatively constant average pore sizes of ~65.8 nm with average wall thickness increasing from 66.8  $\pm$  1.5 nm to 102.1  $\pm$  3.1 nm. As expected, the SAXS patterns shifted to lower q values with increasing material content, consistent with the typical lattice expansion with PMT methods (Fig. 10a). The d-spacing lattice expansion trend was well-fitted with both the 2D and 3D PMT models, each with multiple equivocal combinations of fit parameters that yielded similar quality of fits. Thus the 2D model was presented based on the apparent extent of alignment. The resulting goodness-of-fit  $R^2 = 0.97$  was calculated excluding M:T=1.0 that was again attributed to cylinder jamming (Fig. 10b). Both the ShortCyl and LongCyl series exhibited such deviations from these models with low M:Tvalues which may be studied further in subsequent works and is outside the scope of this study. Regardless, predictable and tailored cylinder-based structures were accessible over a wide range in both cases. For the LongCyl series, the trend for increasing average wall thickness with material: template ratio was also reasonably well-fitted (Fig. 10d). Thus the LongCyl series demonstrated cylindrical pores with independent

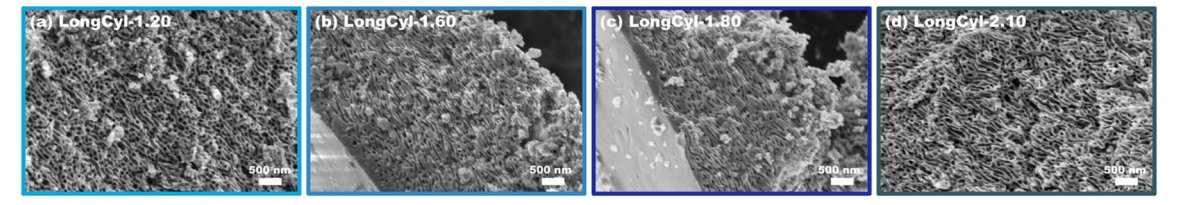


Fig. 9 SEM images of LongCyl series with material: template ratios of: (a) 1.20, (b) 1.60, (c) 1.80, (d) 2.10. The micelles were made using OS1 polymer with agitation.

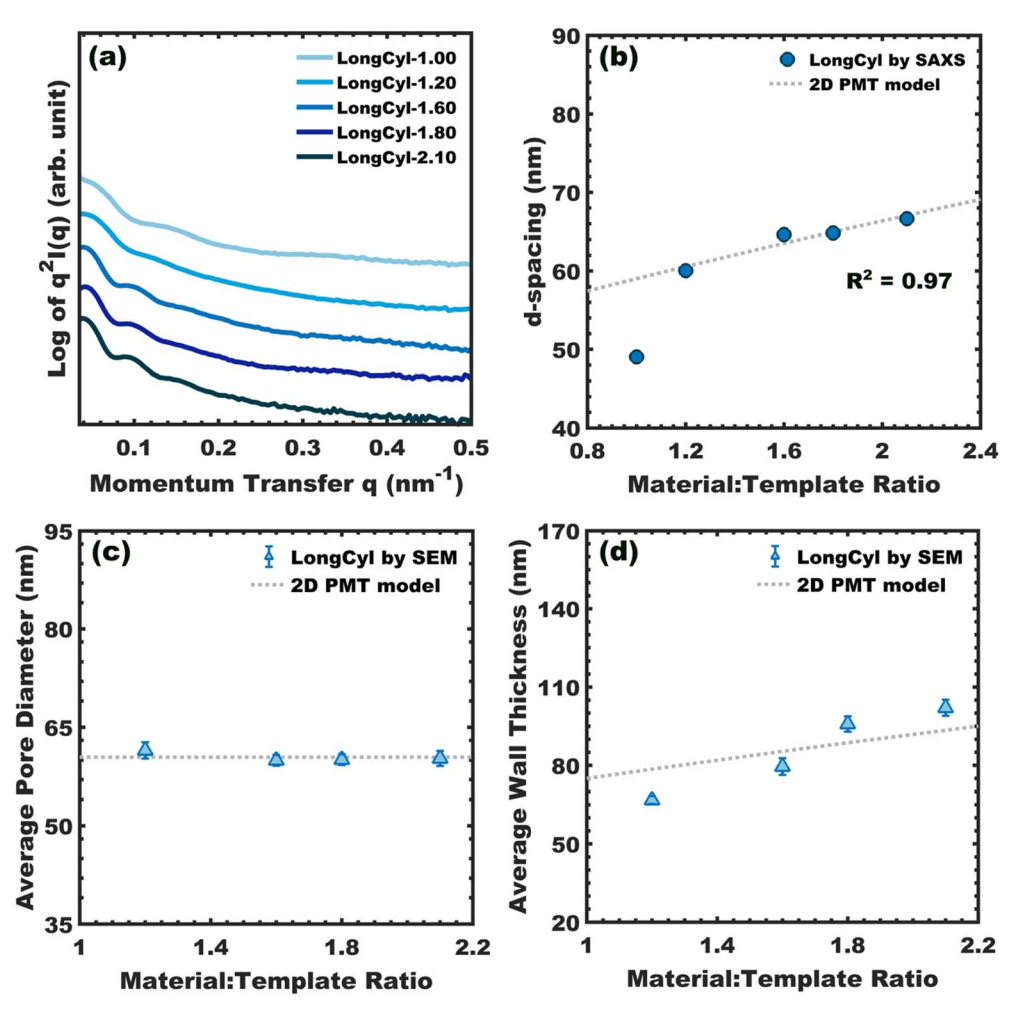


Fig. 10 (a) SAXS data from the LongCyl series where increasing material: template ratio shifted all peaks to lower-q. The (b) d-spacing of the second SAXS peak had minimal overlap with the beam stop and was used to track lattice expansion quantitatively. Similar quality fits were feasible with both the 2D and 3D PMT model where the 2D model is presented corresponding to the increased extent of cylinder alignment (Fig. 8d). The goodness-of-fit was calculated without M:T=1.0 as noted in the manuscript. The average (c) pore diameter and (d) wall thickness were directly measured by SEM. These data demonstrate independent and predictive control of the pore and wall dimensions with aligned cylinders. The micelles were made using OS1 polymer with agitation.

tailoring of the wall thickness dimensions while preserving aligned porosity.

### Conclusion

This study introduces a novel approach using glassy-core cylindrical micelle templates to prepare materials with

cylindrical pores. The use of micelle kinetical entrapment (PMT) enabled independent tailoring of the wall thickness. The use of short cylindrical templates led to limited alignment with significant spread in the distribution of cylinder orientations. A novel agitation induced cylinder growth mechanism was identified that enabled the production of long cylindrical micelles with aspect ratio 15.1 based on apparent micelle fusion

resulting from a novel exchange process. The use of these longer cylindrical micelles as templates led to aligned morphologies without external fields or bias applied (S  $\sim$ 0.92-0.97). The corresponding LongCyl series also enabled independent tailoring of the wall thickness while maintaining aligned porosity. These findings highlight how micelle processing conditions can enable independent feature size adjustment with cylindrical pores combined with tailored extent of alignment based on the cylinder aspect ratio.

#### Author contributions

The manuscript was written through contributions of all authors. All authors have given approval to the final version of the manuscript.

## Conflicts of interest

The authors declare no competing financial interest.

## Data availability

Data for this article, including all SEM, TEM, and SAXS data are available at the Open Science Framework at https://osf.io/9v3t2/ ?view only=3460e775f9344bb983b7b9417511354a.

OS synthesis schemes, NMR and GPC of OS, OS micelle morphologies, ShortCyl aspect ratio, thermo properties (DSC and TGA) of OS, 2D and 3D PMT model fitting parameters of ShortCyls and LongCyls, solvent effect on LongCyls morphology, 2D PMT model and 3D PMT model. See DOI: https://doi.org/10.1039/d5ta04040j.

## Acknowledgements

M. Zhang and M. Stefik acknowledge support from the NSF CAREER program, NSF Award No. DMR-1752615. This work made use of the South Carolina SAXS Collaborative (SCSC). SAXS measurements at UTK are supported by the Major Research Instrument program of the National Science Foundation under Award No. DMR-1827474.

#### References

- 1 S. Y. Yang, J. Park, J. Yoon, M. Ree, S. K. Jang and J. K. Kim, Virus Filtration Membranes Prepared from Nanoporous Block Copolymers with Good Dimensional Stability under High Pressures and Excellent Solvent Resistance, Adv. Funct. Mater., 2008, 18(9), 1371-1377, DOI: 10.1002/ adfm.200700832.
- 2 H. Kosonen, S. Valkama, A. Nykänen, M. Toivanen, G. ten Brinke, J. Ruokolainen and O. Ikkala, Functional Porous Structures Based on the Pyrolysis of Cured Templates of Block Copolymer and Phenolic Resin, Adv. Mater., 2006, 18(2), 201-205, DOI: 10.1002/adma.200401110.
- 3 L. Chen, W. A. Phillip, E. L. Cussler and M. A. Hillmyer, Robust Nanoporous Membranes Templated by a Doubly

- Reactive Block Copolymer, J. Am. Chem. Soc., 2007, 129(45), 13786-13787, DOI: 10.1021/ja0753041.
- 4 P. L. Drzal, A. F. Halasa and P. Kofinas, Microstructure orientation and nanoporous transport gas semicrystalline block copolymer membranes, Polymer, 2000, 41(12), 4671-4677, DOI: 10.1016/S0032-3861(99) 00652-7.
- 5 A. Vu, Y. Qian and A. Stein, Porous Electrode Materials for Lithium-Ion Batteries - How to Prepare Them and What Makes Them Special, Adv. Energy Mater., 2012, 2(9), 1056-1085, DOI: 10.1002/aenm.201200320.
- 6 E. J. W. Crossland, M. Nedelcu, C. Ducati, S. Ludwigs, M. A. Hillmyer, U. Steiner and H. J. Snaith, Block Copolymer Morphologies in Dye-Sensitized Solar Cells: Probing the Photovoltaic Structure-Function Relation, Nano Lett., 2009, 9(8), 2813-2819, DOI: 10.1021/nl800942c.
- 7 W.-S. Young, W.-F. Kuan and T. H. Epps, Block copolymer electrolytes for rechargeable lithium batteries, J. Polym. Sci., Part B: Polym. Phys., 2014, 52(1), 1-16, DOI: 10.1002/ polb.23404.
- 8 R. Watanabe, K. Kamata and T. Iyoda, Smart block copolymer masks with molecule-transport channels for total wet nanopatterning, J. Mater. Chem., 2008, 18(45), 5482-5491, DOI: 10.1039/B806378H.
- 9 M. G. Buonomenna, G. Golemme, C. M. Tone, M. P. De Santo, F. Ciuchi, E. Perrotta, B. Zappone, F. Galiano and Figoli, Ordering phenomena in nanostructured poly(styrene-b-butadiene-b-styrene) (SBS) membranes for selective ethanol transport, J. Membr. Sci., 2011, 385-386, 162-170, DOI: 10.1016/j.memsci.2011.09.035.
- 10 A. K. Jha, L. Chen, R. D. Offeman and N. P. Balsara, Effect of nanoscale morphology on selective ethanol transport through block copolymer membranes, J. Membr. Sci., 2011, 373(1), 112-120, DOI: 10.1016/j.memsci.2011.02.043.
- 11 X.-H. Jin, M. B. Price, J. R. Finnegan, C. E. Boott, J. M. Richter, A. Rao, S. M. Menke, R. H. Friend, G. R. Whittell and I. Manners, Long-range exciton transport in conjugated polymer nanofibers prepared by seeded growth, Science, 2018, 360(6391), 897-900, DOI: 10.1126/science.aar8104.
- 12 J. S. Sakamoto and B. Dunn, Hierarchical battery electrodes based on inverted opal structures, J. Mater. Chem., 2002, 12(10), 2859-2861, DOI: 10.1039/B205634H.
- 13 W. Dong, J. S. Sakamoto and B. Dunn, Electrochemical properties of vanadium oxide aerogels, Sci. Technol. Adv. Mater., 2003, 4(1), 3-11, DOI: 10.1016/S1468-6996(03) 00012-3.
- 14 P. Zhang, L. Wang, S. Yang, J. A. Schott, X. Liu, S. M. Mahurin, C. Huang, Y. Zhang, P. F. Fulvio, M. F. Chisholm, et al., Solid-state synthesis of ordered mesoporous carbon catalysts via a mechanochemical assembly through coordination cross-linking, Commun., 2017, 8(1), 15020, DOI: 10.1038/ncomms15020.
- 15 Y. Mai and A. Eisenberg, Self-assembly of block copolymers, Chem. Soc. Rev., 2012, 41(18), 5969-5985, DOI: 10.1039/ C2CS35115C.

- 16 E. J. W. Crossland, S. Ludwigs, M. A. Hillmyer and U. Steiner, Freestanding nanowire arrays from soft-etch block copolymer templates, *Soft Matter*, 2007, 3(1), 94–98, DOI: 10.1039/B609780D.
- 17 E. J. W. Crossland, P. Cunha, S. Ludwigs, M. A. Hillmyer and U. Steiner, In situ Electrochemical Monitoring of Selective Etching in Ordered Mesoporous Block-Copolymer Templates, ACS Appl. Mater. Interfaces, 2011, 3(5), 1375– 1379, DOI: 10.1021/am2000505.
- 18 E. J. W. Crossland, S. Ludwigs, M. A. Hillmyer and U. Steiner, Control of gyroid forming block copolymer templates: effects of an electric field and surface topography, *Soft Matter*, 2010, 6(3), 670–676, DOI: 10.1039/B914421H.
- 19 E. J. W. Crossland, P. Cunha, S. Scroggins, S. Moratti, O. Yurchenko, U. Steiner, M. A. Hillmyer and S. Ludwigs, Soft-Etch Mesoporous Hole-Conducting Block Copolymer Templates, ACS Nano, 2010, 4(2), 962–966, DOI: 10.1021/ nn901447a.
- 20 A. Sarkar and M. Stefik, Robust porous polymers enabled by a fast trifluoroacetic acid etch with improved selectivity for polylactide, *Mater. Chem. Front.*, 2017, **1**(8), 1526–1533, DOI: **10.1039/C6QM00266H**.
- 21 B. C. Garcia, M. Kamperman, R. Ulrich, A. Jain, S. M. Gruner and U. Wiesner, Morphology Diagram of a Diblock Copolymer–Aluminosilicate Nanoparticle System, *Chem. Mater.*, 2009, 21(22), 5397–5405, DOI: 10.1021/cm901885c.
- 22 M. Stefik, J. Song, H. Sai, S. Guldin, P. Boldrighini, M. C. Orilall, U. Steiner, S. M. Gruner and U. Wiesner, Ordered mesoporous titania from highly amphiphilic block copolymers: tuned solution conditions enable highly ordered morphologies and ultra-large mesopores, *J. Mater. Chem. A*, 2015, 3(21), 11478–11492, DOI: 10.1039/C5TA02483H.
- 23 M. Templin, A. Franck, A. Du Chesne, H. Leist, Y. Zhang, R. Ulrich, V. Schädler and U. Wiesner, Organically Modified Aluminosilicate Mesostructures from Block Copolymer Phases, *Science*, 1997, 278(5344), 1795–1798, DOI: 10.1126/science.278.5344.1795.
- 24 P. C. A. Alberius, K. L. Frindell, R. C. Hayward, E. J. Kramer, G. D. Stucky and B. F. Chmelka, General Predictive Syntheses of Cubic, Hexagonal, and Lamellar Silica and Titania Mesostructured Thin Films, *Chem. Mater.*, 2002, 14(8), 3284–3294, DOI: 10.1021/cm011209u.
- 25 M. Stefik, Single-variable porous nanomaterial series from polymer structure-directing agents, *J. Mater. Res.*, 2022, 37(1), 25–42, DOI: 10.1557/s43578-021-00421-0.
- 26 A. Jain, L. M. Hall, C. B. W. Garcia, S. M. Gruner and U. Wiesner, Flow-Induced Alignment of Block Copolymer– Sol Nanoparticle Coassemblies toward Oriented Bulk Polymer–Silica Hybrids, *Macromolecules*, 2005, 38(24), 10095–10100, DOI: 10.1021/ma0483930.
- 27 P. Bhargava, J. X. Zheng, P. Li, R. P. Quirk, F. W. Harris and S. Z. D. Cheng, Self-Assembled Polystyrene-blockpoly(ethylene oxide) Micelle Morphologies in Solution, *Macromolecules*, 2006, 39(14), 4880–4888, DOI: 10.1021/ ma060677s.

- 28 L. Luo and A. Eisenberg, One-Step Preparation of Block Copolymer Vesicles with Preferentially Segregated Acidic and Basic Corona Chains, *Angew. Chem., Int. Ed.*, 2002, 41(6), 1001–1004, DOI: 10.1002/1521-3773(20020315) 41:6<1001::AID-ANIE1001>3.0.CO;2-Q.
- 29 L. Zhang and A. Eisenberg, Thermodynamic vs. Kinetic Aspects in the Formation and Morphological Transitions of Crew-Cut Aggregates Produced by Self-Assembly of Polystyrene-b-poly(acrylic acid) Block Copolymers in Dilute Solution, *Macromolecules*, 1999, 32(7), 2239–2249, DOI: 10.1021/ma981039f.
- 30 P. Bhargava, Y. Tu, J. X. Zheng, H. Xiong, R. P. Quirk and S. Z. D. Cheng, Temperature-Induced Reversible Morphological Changes of Polystyrene-block-Poly(ethylene Oxide) Micelles in Solution, J. Am. Chem. Soc., 2007, 129(5), 1113–1121, DOI: 10.1021/ja0653019.
- 31 K. Yu, C. Bartels and A. Eisenberg, Trapping of Intermediate Structures of the Morphological Transition of Vesicles to Inverted Hexagonally Packed Rods in Dilute Solutions of PS-b-PEO, *Langmuir*, 1999, **15**(21), 7157–7167, DOI: **10.1021/la981688k**.
- 32 X. X. Zhu, K. Banana and R. Yen, Pore Size Control in Cross-Linked Polymer Resins by Reverse Micellar Imprinting, *Macromolecules*, 1997, **30**(10), 3031–3035, DOI: **10.1021**/ **ma961580g**.
- 33 K. T. Lee and S. M. Oh, Novel synthesis of porous carbons with tunable pore size by surfactant-templated sol-gel process and carbonisation, *Chem. Commun.*, 2002, (22), 2722–2723, DOI: 10.1039/B208052D.
- 34 C. Matei Ghimbeu, L. Vidal, L. Delmotte, J.-M. Le Meins and C. Vix-Guterl, Catalyst-free soft-template synthesis of ordered mesoporous carbon tailored using phloroglucinol/glyoxylic acid environmentally friendly precursors, *Green Chem.*, 2014, 16(6), 3079–3088, DOI: 10.1039/C4GC00269E.
- 35 P. M. Lipic, F. S. Bates and M. A. Hillmyer, Nanostructured Thermosets from Self-Assembled Amphiphilic Block Copolymer/Epoxy Resin Mixtures, *J. Am. Chem. Soc.*, 1998, 120(35), 8963–8970, DOI: 10.1021/ja981544s.
- 36 Y. Meng, D. Gu, F. Zhang, Y. Shi, L. Cheng, D. Feng, Z. Wu, Z. Chen, Y. Wan, A. Stein, *et al.*, A Family of Highly Ordered Mesoporous Polymer Resin and Carbon Structures from Organic–Organic Self-Assembly, *Chem. Mater.*, 2006, **18**(18), 4447–4464, DOI: **10.1021/cm060921u**.
- 37 C. Cai, L. Wang, J. Lin and X. Zhang, Morphology Transformation of Hybrid Micelles Self-Assembled from Rod-Coil Block Copolymer and Nanoparticles, *Langmuir*, 2012, 28(9), 4515-4524, DOI: 10.1021/la204941w.
- 38 J. Massey, K. N. Power, I. Manners and M. A. Winnik, Self-Assembly of a Novel Organometallic-Inorganic Block Copolymer in Solution and the Solid State: Nonintrusive Observation of Novel Wormlike Poly(ferrocenyldimethylsilane)-b-Poly(dimethylsiloxane) Micelles, J. Am. Chem. Soc., 1998, 120(37), 9533–9540, DOI: 10.1021/ja981803d.
- 39 J. B. Gilroy, T. Gädt, G. R. Whittell, L. Chabanne,J. M. Mitchels, R. M. Richardson, M. A. Winnik andI. Manners, Monodisperse cylindrical micelles by

- crystallization-driven living self-assembly, Nat. Chem., 2010, 2(7), 566-570, DOI: 10.1038/nchem.664.
- 40 H. Wang, W. Lin, K. P. Fritz, G. D. Scholes, M. A. Winnik and I. Manners, Cylindrical Block Co-Micelles with Spatially Selective Functionalization by Nanoparticles, J. Am. Chem. Soc., 2007, 129(43), 12924-12925, DOI: 10.1021/ja075587x.
- 41 N. Petzetakis, A. P. Dove and R. K. O'Reilly, Cylindrical micelles from the living crystallization-driven self-assembly of poly(lactide)-containing block copolymers, Chem. Sci., 2011, 2(5), 955-960, DOI: 10.1039/C0SC00596G.
- 42 M. C. Arno, M. Inam, Z. Coe, G. Cambridge, L. J. Macdougall, R. Keogh, A. P. Dove and R. K. O'Reilly, Precision Epitaxy for Aqueous 1D and 2D Poly(ε-caprolactone) Assemblies, J. Am. Chem. Soc., 2017, 139(46), 16980-16985, DOI: 10.1021/ jacs.7b10199.
- 43 D. Tao, C. Feng, Y. Cui, X. Yang, I. Manners, M. A. Winnik and X. Huang, Monodisperse Fiber-like Micelles of Controlled Length and Composition with an Oligo(pphenylenevinylene) Core via "Living" Crystallization-Driven Self-Assembly, J. Am. Chem. Soc., 2017, 139(21), 7136-7139, DOI: 10.1021/jacs.7b02208.
- 44 K. A. Lantz, N. B. Clamp, W. van den Bergh, A. Sarkar and M. Stefik, Full Gamut Wall Tunability from Persistent Micelle Templates via Ex Situ Hydrolysis, Small, 2019, 15(18), 1900393, DOI: 10.1002/smll.201900393.
- 45 A. Sarkar and M. Stefik, How to make persistent micelle templates in 24 hours and know it using X-ray scattering, J. Mater. Chem. A, 2017, 5(23), 11840–11853, DOI: 10.1039/ C7TA01034F.
- 46 E. R. Williams, P. L. McMahon, J. E. Reynolds, J. L. Snider, V. Stavila, M. D. Allendorf and M. Stefik, Tailored porous carbons enabled by persistent micelles with glassy cores, Mater. Adv., 2021, 2(16), 5381–5395, DOI: 10.1039/ D1MA00146A.
- 47 E. Törnguist, L. Gentile, S. Prévost, A. Diaz, U. Olsson and H. Isaksson, Comparison of small-angle neutron and X-ray scattering for studying cortical bone nanostructure, Sci. Rep., 2020, 10(1), 14552, DOI: 10.1038/s41598-020-71190-9.
- 48 W. van den Bergh and M. Stefik, Understanding Rapid Intercalation Materials One Parameter at a Time, Adv. Funct. Mater., 2022, 32(31), 2204126, DOI: 10.1002/ adfm.202204126.
- 49 J. De Yoreo, D. Mandrus, L. Soderholm, T. Forbes, M. Kanatzidis, J. Erlebacher, J. Laskin, U. Wiesner, T. Xu, and S. Billinge, Basic Research Needs Workshop on Synthesis Science for Energy Relevant Technology, USDOE Office of Science (SC), United States, 2016.
- 50 M. Stefik, S. Mahajan, H. Sai, T. H. Epps, III, F. S. Bates, S. M. Gruner, F. J. DiSalvo and U. Wiesner, Ordered Threeand Five-ply Nanocomposites from ABC Block Terpolymer Microphase Separation with Niobia and Aluminosilicate Sols, Chem. Mater., 2009, 21(22), 5466-5473, DOI: 10.1021/ cm902626z.
- 51 H. N. Lokupitiya, A. Jones, B. Reid, S. Guldin and M. Stefik, Ordered Mesoporous to Macroporous Oxides with Tunable Isomorphic Architectures: Solution Criteria for Persistent

- Micelle Templates, Chem. Mater., 2016, 28(6), 1653-1667, DOI: 10.1021/acs.chemmater.5b04407.
- 52 A. Sarkar, L. Evans and M. Stefik, Expanded Kinetic Control for Persistent Micelle Templates with Solvent Selection, Langmuir, 2018, 34(20), 5738-5749, DOI: **10.1021**/ acs.langmuir.8b00417.
- 53 A. Sarkar, A. Thyagarajan, A. Cole and M. Stefik, Widely tunable persistent micelle templates via homopolymer swelling, Soft Matter, 2019, 15(26), 5193-5203, DOI: 10.1039/C9SM00484J.
- 54 E. R. Williams, C. X. Ruff and M. Stefik, Unimer suppression enables supersaturated homopolymer swollen micelles with long-term stability after glassy entrapment, Soft Matter, 2024, 20(10), 2288-2300, DOI: 10.1039/D3SM01754K.
- 55 J. Yuan, Z. Xu, S. Cheng and L. Feng, The aggregation of polystyrene-b-poly(ethylene oxide)-b-polystyrene triblock copolymers in aqueous solution, Eur. Polym. I., 2002, 38(8), 1537-1546, DOI: 10.1016/S0014-3057(02)00025-3.
- 56 C. Luo, X. Han, Y. Gao, H. Liu and Y. Hu, Aggregate Morphologies of PS-b-PEO-b-PS Copolymer in Mixed Solvents, J. Dispersion Sci. Technol., 2011, 32(2), 159-166, DOI: 10.1080/01932690903546843.
- 57 R. P. Murphy, E. G. Kelley, S. A. Rogers, M. O. Sullivan and T. H. Epps III, Unlocking Chain Exchange in Highly Amphiphilic Block Polymer Micellar Systems: Influence of Agitation, ACS Macro Lett., 2014, 3(11), 1106-1111, DOI: 10.1021/mz500435d.
- 58 E. G. Kelley, R. P. Murphy, J. E. Seppala, T. P. Smart, S. D. Hann, M. O. Sullivan and T. H. Epps, Size evolution of highly amphiphilic macromolecular solution assemblies via a distinct bimodal pathway, Nat. Commun., 2014, 5(1), 3599, DOI: 10.1038/ncomms4599.
- 59 H. N. Lokupitiya and M. Stefik, Cavitation-enabled rapid and tunable evolution of high-χN micelles as templates for ordered mesoporous oxides, Nanoscale, 2017, 9(4), 1393-1397, DOI: 10.1039/C6NR07313A.
- 60 K. A. Lantz, A. Sarkar, K. C. Littrell, T. Li, K. Hong and M. Stefik, Cavitation Enables Switchable and Rapid Block Polymer Exchange under High-γN Conditions, Macromolecules, 2018, 51(17), 6967-6975, DOI: 10.1021/ acs.macromol.8b01244.
- 61 T. Larison, E. Williams, C. S. Collins, S. V. Pingali and M. Stefik, Bimodal Rates for Cavitation-Induced Chain Exchange Between Micelles, Macromolecules, 2023, 56(19), 7818-7826, DOI: 10.1021/acs.macromol.3c01040.
- 62 T. P. Lodge, C. L. Seitzinger, S. C. Seeger, S. Yang, S. Gupta and K. D. Dorfman, Dynamics and Equilibration Mechanisms in Block Copolymer Particles, ACS Polym. Au, 2022, 2(6), 397–416, DOI: 10.1021/acspolymersau.2c00033.
- 63 J. Zhao, S. Li, R. Zou and A. Yu, Dense random packings of spherocylinders, Soft Matter, 2012, 8(4), 1003–1009, DOI: 10.1039/C1SM06487H.
- 64 C. Ferreiro-Córdova and J. S. van Duijneveldt, Random Packing of Hard Spherocylinders, J. Chem. Eng. Data, 2014, 59(10), 3055-3060, DOI: 10.1021/je500119r.